Electrically Induced Directional Ion Migration in Two-Dimensional Perovskite Heterostructures

Jee Yung Park[1,8], Yoon Ho Lee[1,2,3,8], Md Asaduz Zaman Mamun[4], Mir Md Fahimul Islam[4], Shuchen Zhang[1], Ke Ma[1,2], Aalok Uday Gaitonde[5], Kang Wang[1,6], Seok Joo Yang[1], Amy Marconnet[5], Jianguo Mei[2], Muhammad Ashraful Alam[4], Letian Dou[1,2,7,9*]

[1]Davidson School of Chemical Engineering, Purdue University, West Lafayette, IN 47907, United States.

[2]Department of Chemistry, Purdue University, West Lafayette, IN 47907, United States.

[3]Department of Environment and Energy Engineering, Sungshin Women's University, Seoul 01133, Republic of Korea.

[4]Elmore Family School of Electrical and Computer Engineering, Purdue University, West Lafayette, IN 47907, United States.

[5]School of Mechanical Engineering, Purdue University, West Lafayette, IN 47907, United States.

[6]Key Laboratory of Photochemistry, Institute of Chemistry Chinese Academy of Sciences, Beijing 100190, China.

[7]Birck Nanotechnology Center, Purdue University, West Lafayette, IN 47907, United States.

[8]These authors contributed equally.

[9]Lead contact

[*]Correspondence: dou10@purdue.edu (L.D.)

Summary

Understanding ion migration in two-dimensional (2D) perovskite materials is key to enhancing halide perovskite device performance and stability. However, prior studies have been primarily limited to heat and light induced ion migration. In this work, to investigate electrically induced ion migration in 2D perovskites, we construct a high-quality single crystal 2D perovskite heterostructure device platform with near defect-free van der Waals contact. While achieving real-time visualization of halide anions migrating towards the positive bias, defined here as directional ion migration, we also uncover the unique behavior of halide anions inter-diffusing towards the opposite direction under prolonged bias. Confocal microscopy imaging reveals a halide migration channel that aligns with the crystal and heterojunction edges. After a sustained ion migration, stable junction diodes exhibiting up to ~1000-fold forward to reverse current ratio are realized. This study unveils important fundamental insights on halide migration under electrical bias, paving the way towards high-performance devices.

Introduction

Halide perovskite optoelectronics have shown remarkable progress over the past decade, attributed to their solution-processability and significant optoelectronic properties.[1–3] However, their inherent instability due to the ionic nature of the soft halide perovskite lattice is an obstacle for long-term use, particularly because of ion migration.[4,5] This can be triggered by factors such as heat, light, electric field, or current during operation, leading to issues such as current-voltage hysteresis, transport layer doping, and accelerated material degradation.[6–9] Additionally, mobile ions can cause further problems like phase segregation in mixed-halide systems.[10–12] To overcome these challenges, two-dimensional (2D) perovskites with hydrophobic organic cations have emerged as a more stable alternative to three-dimensional (3D) perovskites.[13–15] Recently, efficient optoelectronic devices utilizing quasi-2D perovskites or 2D-3D perovskite heterostructures have been demonstrated, spurring innovations in this field and heightening interest in understanding ion migration behavior, particularly in 2D perovskites.[16,17]

Research on ion migration has been mostly focused on single component polycrystalline thin films or single crystals which pose challenges in direct visualization of ion movement under an external stimulus.[18,19] Heterostructures can work as a promising platform, offering clearer visualization and allowing more precise quantification through observation of ion migration across interfaces. While previous works utilizing heterostructures have mainly focused on heat or light induced migration and phase segregation, ion migration in heterostructures under electric bias has not been well investigated, due to the challenges in reliable device fabrication, particularly lacking studies based on 2D perovskites.[20–24] In this work, we construct high-quality 2D perovskite single crystal heterostructure devices with van der Waals contact established through multi-step dry transfer. This approach allows us to visualize real-time migration of halide anions towards the positive bias, an observation we define as directional ion migration, revealing new insights into the behavior of halide anions under electric bias. Key findings include the discovery of vacancy-induced inter-diffusion against bias direction and an analysis of preferred ion migration pathways, showing that ion migration is not only directional but also favored along the edges of single crystal sheets, which is completely different from thermally induced ion diffusion. These directional ion migration behaviors are also validated through a simulation which replicates similar ion movement under the influence of electric field. Moreover, ion migration in 2D perovskite heterostructure devices results in a unique diode behavior, with particularly amplified performance in double junctions. Our study establishes important insights regarding electrically induced ion migration with a simple yet powerful heterostructure platform, which can be further utilized for potential in-depth studies and device integration.

Results and Discussion

Fabrication of single crystal heterostructure devices

Heterostructures of single crystals are fabricated through a step-by-step dry transfer of 2D perovskite single crystal sheets incorporating phenylethyl ammonium (PEA) cations, which are acquired via a floating growth method that enables the synthesis of large area, high-quality sheets.[25] As depicted in **Figure 1A**, a mildly heated saturated precursor solution is dropped onto a glass plate, initiating the crystallization of single crystal sheets at the air-solution interface. Crystal sheets are then retrieved with

polydimethylsiloxane (PDMS) attached to a glass slide and dried in a vacuum chamber for dry transfer preparation. Three different crystal sheets, **Br n=1** ($(PEA)_2PbBr_4$), **I n=1** ($(PEA)_2PbI_4$), and **I n=2** ($(PEA)_2(MA)Pb_2I_7$) were synthesized as building blocks for the heterostructures. **Figure S1** shows the typical optical images of the prepared single crystal sheets on PDMS. The thickness was measured to be in the 50 ~ 150 nm range as measured in **Figure S2**. Then, as illustrated in **Figures 1B-D**, 2D perovskite crystal sheets are transferred onto a Si/SiO_2 substrate with Ti/Au contact pads, prepared via photolithography. Consecutive point-to-point transfers are executed using a transfer stage to create a bromide-iodide heterostructure. This design includes an overlapping area between the two crystal sheets, enabling halide anions to migrate across the heterostructure. The heterostructure is constructed in between two Ti/Au pads which would later serve as a secondary contact pad for electrical measurements.

Br n=1 – I n=1 heterostructures were characterized to ensure the phase purity of the pristine samples. **Figure 1E-H** shows a scanning electron microscopy (SEM) image of the junction area and the corresponding energy-dispersive X-ray spectroscopy (EDS) elemental mappings of bromine, iodine, and lead, clearly indicating distinct elemental distribution within the pristine heterostructure. **Figure 1I-K** provides optical images and confocal photoluminescence (PL) mapping images detecting two different wavelength ranges of 410 - 440 nm and 500 - 530 nm, which display a clear distribution of PL emission with sharp boundaries. PL spectra shown in **Figure 1L** also presents the emission wavelength of both **Br n=1** and **I n=1** crystal sheets, absent of an alloy phase PL peak. X-ray diffraction (XRD) patterns of perovskite single crystals (**Br n=1**, **I n=1**, **I n=2**) and heterostructures (**Br n=1 – I n=1**, and **Br n=1 – I n=2**) are also compared in **Figure S3**, which proves the formation of a sharp junction between two pure crystal sheets with minimal alloy formation. Additionally, **Figure S4** provides more optical and PL images of heterostructures with different configurations showing the robustness of this method.

Further development of these pristine heterostructures into a device platform involves applying a unique electrode dry-transfer method, as illustrated in **Figure 2A**. Two Au electrodes with a channel gap of 20 ~ 40 μm and attached to polymethyl methacrylate (PMMA), are dry transferred onto the pristine heterostructure. This transfer is executed

using a thermal release tape, which requires heating to lose adhesion.[26,27] The transfer process is conducted with great precision to ensure that the junction part is strategically positioned in the channel between the two electrodes and that each Au electrode can establish contact with the pre-patterned Ti/Au pads. This channel gap, which uncovers the junction area, will later serve as a window for observing ion movement. The Ti/Au pads play a critical role in forming reliable contact with the electrical measurement probes, ensuring consistent results even with repeated measurements. Meanwhile, the PMMA functions as a transparent protection layer, isolating the interference of moisture and oxygen, increasing the overall stability of the device. **Figure 2B** provides a cross-sectional schematic representation of the device's configuration after the completion of all dry-transfer steps, accompanied with the top view of a real device with low magnification shown in **Figure S5**.

Electrically induced directional halide migration

Fabricated heterostructure devices were induced with electric bias to investigate the ion migration behavior. Ion migration was analyzed through real-time PL imaging of the junction area. Movement of bromide anions into the iodide region, or vice versa, would result in alloy formation, giving rise to a new PL emission peak that locates between the pure bromide and iodide perovskites emission wavelength. Two different **Br n=1 – I n=1** heterostructure devices with a similar configuration was prepared to contrast the ion migration behavior under varying directions of electric bias. An electric bias of 5 V was applied for 5 minutes to both devices, as shown in **Figures 2C-F**, the only distinction being the direction of the bias. The heterostructures did not show any notable changes with electric bias lower than 5 V. **Figures 2C and 2E** show optical and PL images of the heterostructure devices before introducing bias. **Figures 2D and 2F** are the PL images following the electric bias treatment, and corresponding confocal PL mapping images are included in **Figures S6 and S7**. Notably, when the electric field is directed towards **Br n=1**, no significant alteration in the PL image is observed before and after the bias, as observed in **Figures 2C and 2D**. However, in the opposite case, a pronounced change in PL image is observed as migration of iodide anion is triggered towards the **Br n=1** side due to the electric stimulus, forming an I/Br alloy. As iodide anions carry a negative charge, they can only migrate to the **Br n=1** area only if the electric field is oriented towards the **I n=1** side. On the other hand, bromide

anions can only migrate to the **I n=1** area if the electric field is oriented towards the **Br n=1** side. In this work, we define such movement of halide anion as directional ion migration, where the ions move towards a specific direction guided by the induced electric field. It should be acknowledged that the movement of bromide anions in **Figure 2D** is happening but is not observable as the **Br n=1** sheet is covered by the **I n=1** sheet in the junction area. Thus, the movement of iodine was only of focus here for varying electric field directions, considering that band shift is more abrupt with iodine moving to the bromide area and photoluminescence quantum yield (PLQY) is generally higher for iodine rich phases. Clear demonstration of directional ion migration behavior in heterostructures when subjected to electric stimuli can also be confirmed through a real-time video recording of PL image evolution shown in **Supplemental Videos 1 and 2**. Furthermore, even after the external bias was turned off after ion migration, the Br/I alloy PL emissions largely persisted as seen in **Figure S8** showing only partial relaxation of anions back towards their origin.

To further investigate the directional migration behavior under a more potent electric stimulus, a larger bias was applied for an extended time duration. **Figure 2G** shows the optical and PL image of the **Br n=1 – I n=1** heterostructure device in its pristine state. Induced with 20 V of electric bias, **Figures 2H and 2I** show two PL images with an interval of 10 mins. To precisely identify the spatial distribution of Br/I alloy formation due to ion migration, confocal PL mapping images in the wavelength range of 490 nm – 510 nm were captured as shown in the lower panels of **Figures 2H and 2I**. With the application of a stronger electric bias to the heterostructure, directional ion migration occurs simultaneously with partial degradation. The ion migration behavior is directly observable from a real-time PL image video provided in **Supplemental Video 3**, where the **I n=1** sheet is gradually transformed into a sky-blue Br/I phase due to ion migration while its boundary keeps shifting towards the positive bias. **Figure 2H**, showing the heterostructure after 10 mins of bias, reveals the formation of alloy phase and shift of boundary. As the electric bias continues, the alloy phase boundary progresses towards the cathode, as displayed in **Figure 2I**. The PL emission peaks from the junction area after 10 mins and 20 mins exhibit a clear emergence of a Br/I alloy peak around the 490 – 510 nm range as seen in **Figure 2J**. Moreover, the alloy peak after 20 minutes

displays a relative blue shift with an increased intensity, indicative of a rising ratio of bromide to iodide in the alloy phase.

In addition, it is worth noting that as the progression of the Br/I alloy towards the positive bias continues over time, **Br n=1** sheet also begins to exhibit Br/I alloy phase PL emissions as well, indicated by **Figure 2l**. This is an unexpected behavior as this requires iodide anions, a negatively charged particle, to migrate towards negative bias. The confocal PL mapping image in **Figure 2l** provides further evidence that the Br/I alloy has emerged in the **Br n=1** crystal sheet. Full collection of confocal PL mapping images of different wavelength pockets is provided in **Figures S9 and S10**. The initial directional migration of bromide anions, followed by the migration of iodide anions in the opposing direction can be explained by the proposed mechanism illustrated in the schematic shown in **Figure 2K**. Initially, when a **Br n=1 – I n=1** heterostructure is induced with an electric bias (positive bias on the **I n=1** side and negative bias on the **Br n=1** side), this causes both iodide and bromide anions to migrate towards the positive bias, simultaneously forming a Br/I alloy phase. Then, when a strong enough bias is sustained, continuous ion migration leads to increased bromide vacancies in vicinity of the anode. This creates a large enough gradient of halide vacancy concentration within the heterostructure, instigating a vacancy-driven interdiffusion of iodide anions to fill the voids in the **Br n=1** sheet. It can also be understood that halide oxidation and reabsorption may play a role as well according to previous studies.[10,11] Consequently, this results in the formation of Br/I alloy phase near the anode and the gradual evolution showing the change in spatial distribution of Br/I alloy PL emission in **Supplemental Video 3** supports the proposed ion migration behavior as well.

Ion mobility values and diffusion coefficients were calculated and compared with previous reports that quantify these parameters using various platforms featuring halide perovskite materials. The interrelation between ion mobility and diffusion coefficient is established by the following Einstein relation:[28,29]

$$\boldsymbol{D = \frac{\mu\, k_B\, T}{q}}\,, \boldsymbol{\mu = \frac{v}{E}}$$

where D is diffusion coefficient, μ is ion mobility, k_B is Boltzmann constant, T is absolute temperature, q is electrical charge on the electron, v is the ion drift velocity

and E is the electrical field applied to the material. **Figure S11** provides a schematic on how ion mobility and diffusion coefficient was calculated from the **Br n=1 – I n=1** heterostructure along with the distribution of calculated values. **Figure S12a** compares this work's ion mobility values with earlier studies that investigate ion migration in 3D perovskite devices.[20,22,30–32] Meanwhile, **Figure S12b** compares diffusion coefficient values with previous studies that investigate ion migration in 2D and 3D perovskites.[23,33–36] Heightened mobility and diffusion coefficient values in this work can be attributed to the enhanced electrical current densities passing through the crystals enabled by the high-quality van der Waals contact devices, resulting in higher vacancy/defect densities. High current levels were recorded during ion migration experiments (**Figure S13**). Momentum of electrons flowing through the material transferred to the lattice can lead to electromigration, increasing defect density in the lattice, subsequently contributing to elevated mobility and diffusion coefficient values in the heterostructure devices.[37]

Halide ion migration pathways

As observed in **Figures 2G-2I**, it's important to recognize that ion migration is not a random process; rather, it typically originates from the corners near the junction area and favors propagation along the edge region over the bulk region of the crystal sheets. **Br n=1 – I n=2** heterostructures were utilized to further confirm directional ion migration and illuminate the preferred migration pathways, as well as to uncover the driving forces governing electrically driven ion migration in 2D perovskites. **I n=2** crystal sheets comprised of two inorganic octahedral layers with an increased amount of iodide anions per volume compared to **I n=1**, yield two specific advantages. Firstly, they allow the initiation of ion migration with a relatively smaller electric bias and a shorter time duration due to their relative abundance in halide anions, facilitating the revelation of preferred migration pathways. Secondly, the differentiation between the Br/I alloy PL emission (green) and the pure PL emission wavelengths from **Br n=1** (blue) and **I n=2** (orange) becomes more discernible. This contrast enhances real-time PL mapping, making the analysis more convenient and informative. **Figure S14** shows the PL spectra of the heterostructure junction area, both in its pristine state and after the application of electric bias.

Both optical and PL images (**Figures 3A and 3B**) of a **Br n=1 – I n=2** heterostructure were collected before and after it was subjected to an electric bias of 3 V for a duration of 5 minutes. The heterostructure did not exhibit notable changes under electric bias under 3 V. What stands out is the exclusive formation of the alloy phase along the edge of the junction area, highlighted by a directed migration of iodide anions only towards the **Br n=1** crystal sheet. This behavior is distinctly different from thermally induced anion diffusion, which results in a uniform alloy formation across the entire junction area, featured in **Figure S15**. Confocal PL mapping in the lower panel of **Figure 3B** further reveals alloy formation specifically in the edge connecting the cathode and **I n=2** crystal sheet, further supporting that ion migration is more concentrated in the edge region. The full collection of confocal PL mapping images across different wavelength pockets is available in **Figure S16**. To validate the directionality and edge-focused ion migration pathway, a double junction with an **I n=2 – Br n=1 – I n=2** heterostructure was also fabricated and tested using an identical electric bias. As shown in **Figure 3C**, the results were consistent with the green Br/I alloy formation localized on the edges of the crystal sheets within the heterostructure. Interestingly, both iodide and bromide anions migrated towards the right side, leaving the opposite edges devoid of alloy formation. This unique pattern was captured in the PL image and confocal PL mapping image in **Figure 3D**. A complete set of confocal PL mapping images can be found in **Figure S17**. These findings are also further supported by previous studies reporting grain boundary dominant ion migration in halide perovskites thin films.[38,39]

To further uncover the effects that electric bias may have on the edge region and why it may facilitate an ion migration pathway, an analysis of electric current in the heterostructure devices was performed. **Figure S18** shows the optical and PL image of a device platform created specifically to perform spatial mapping of electric current flow in a single crystal sheet. In these mappings, the edge regions were revealed to be more conductive, exhibiting higher current values compared to the bulk region. An earlier study by Wang et al. using similar means of measurement on 2D perovskites have also shown similar conclusions concerning edge conductivity.[40] As higher electric current levels in the edges can increase the local defect density in the lattice due to stronger electromigration effects, it consequently becomes a preferred channel for

halide anion migration. **Figures S19 and S20** as well as **Supplemental Videos 4 and 5** also show additional heterostructures revealing edge focused ion migration channels. To rule out any other major factors, especially resistive Joule heating in particular, which might trigger thermally induced ion migration, an infrared microscope was used to obtain spatial temperature mapping of the heterostructure device while electric bias was applied. As shown in **Figure S21**, the heterostructure showed minimal temperature change from room temperature conditions. To further confirm, a heterostructure device with a junction perpendicular to two electrodes were fabricated and induced with 40 V of electric bias. As provided in **Supplemental Video 6** and **Figure S22**, the heterostructure showed no thermal diffusion or ion migration across the junction even until degradation which proves that ion migration in the heterostructures happen solely due to electric bias and current in the platforms we created.

Electric field and ion transport simulations were also conducted to corroborate the ion migration behavior observed in experiments. **Br n=1 – I n=1** heterostructure platform was utilized to model the electric field and mobile ion concentration evolution over time through theoretical calculations (see Methods for details). **Figure 3E** illustrates three selected points across the heterostructure's cross-section for analysis. Among the three points, points 1 and 3 represent the junction edge regions adjacent to Br n=1 and I n=1 side respectively, while point 2 represents the bulk region of the junction. The electric field at points 1 and 3 exhibited notably higher absolute values in the x and y components near the heterostructure interface, as depicted in **Figure 3F**. As the y component of the electric field governs the anions migrating across the heterostructure interface, this explains the more profound migration of ions in the junction edge regions compared to the bulk region, as observed in the experiments. Thus, as illustrated in **Figure 3G and 3H** bromide concentration at points 1 and 3 initially surged across the interface enabled by the active ion migration driven by the initial electric field, followed by a slight decline as ions migrate laterally. In contrast, point 2 displayed a consistent and gradual but relatively slower increase in bromide concentration, attributed to a weaker electric field. **Figure S23** presents the iodide concentration evolution, revealing an accumulation against the induced bias before inter-diffusion after a certain time. Initially hindered by an unfavorable electric field,

iodide ions eventually migrated when vacancies on the opposite side induced a sufficient screening effect, coupled with a steepened anion concentration gradient across the junction.

Post-migration diode behavior

When the heterostructure devices were applied with a consistent bias in a single direction as illustrated in **Figure 4A**, a unique change in device characteristics was revealed. Initially, these devices displayed a standard current-voltage (*I-V*) curve, akin to that of a typical halide perovskite material with symmetric electrodes. Yet, under a sustained bias of 3 V, they began to demonstrate a diode-like behavior, as depicted in **Figures 4B and 4C**. The *I-V* curve's evolution in relation to the bias duration is shown in **Figure S24**, showing that the forward current level increases significantly with more time the heterostructure is applied with a sustained bias. Also, *I-V* curves of non-heterostructure devices with a single crystal sheet showed symmetrical behavior under forward and reverse bias as shown in **Figure S25**, supporting that the diode behavior can be attributed to ion migration triggered by external electric bias rather than the intrinsic property of the material. As presented in **Figure 4A**, persisted migration of halide anions in one direction can result in the formation of asymmetrically distributed vacancy and interstitial defects. It's reported that point defects possess shallow energy levels in 3D halide perovskites as well as 2D perovskites.[41,42] Thus, the asymmetric nature of these point defects (interstitials and vacancies) across the junction may lead to self-doping, resulting in the formation of a P-N junction.[43] To further investigate how the diode behavior rises, device simulations were performed using analytical equations (see Methods for details). **Figures 4F and 4G** show the fitted device simulation *I-V* curves for reverse bias and forward bias, respectively. As the diode operates at a significantly lower turn-on voltage compared to conventional diodes while showing higher reverse leakage currents, this can be attributed to the soft breakdown of the diode.[44,45] As shown in **Figure 4H**, electron and hole hopping can occur during forward and reverse biasing due to an abundance of point defects in the junction. The asymmetricity of the current in both directions is also contributed by the disparity in the bandgap between the two components.

While there are reports of ion migration induced diode behavior in 3D halide perovskites, often referred to as poling effects, the 2D perovskite heterostructures examined in this study set themselves apart by consistently maintaining this state, even with repeated cycles, as demonstrated in **Figure S26**.[4,46] This contrasts with 3D perovskite materials, which struggle to sustain the poled state over extended periods. Due to the organic cation barriers between inorganic layers, reversing active ion migration across distinct layers in 2D perovskite materials isn't feasible. Overall, as previous poling studies are rather a display of pseudo-junctions from single materials, 2D perovskite heterostructures in this work are inherent junctions of two layers with different halide species which transform into a junction diode. Moreover, double junction heterostructures displayed heightened diode characteristics, exhibiting a remarkable ~1000-fold forward and reverse current ratio at 4V as shown in **Figures 4D and 4E**, pointing to the potential for enhancing diode performance by tweaking heterostructure configurations. The junction diodes created also displayed evidence of photovoltaic effect with a clear open-circuit voltage under light excitation as displayed in **Figure S27**. The stability of these junctions, coupled with the adaptable diode properties through heterostructure setup, reveals a promising avenue for further exploration in semiconductor device application.

Conclusion

In summary, we have fabricated a 2D perovskite single crystal heterostructure device with Van der Waals contact, achieved through a multi-step dry transfer technique to conduct a comprehensive study of ion migration under the influence of an electric bias. Accompanied by real-time visualization of PL and confocal spatial mapping of Br/I alloy phases, highly directional ion migration behavior was observed. Heterostructure under different electric bias conditions elucidated not only directional ion migration but also vacancy-driven interdiffusion of anions in an electrically unfavored direction due to sufficient vacancy accumulation. It was also revealed that ion migration favors the edge regions of crystal sheets, attributed to higher electrical conductivity in the edge. We further corroborated these ion migration patterns through simulations that assessed the evolution of electric fields and ion concentrations in different sections of the heterostructure. Additionally, the transformation of the heterostructure into a stable junction diode was another significant outcome, observed after sustained directional

ion migration, leading to improved diode characteristics in double junction heterostructure devices. Overall, our research sheds light on the dynamics of electrically stimulated ion migration and its implications for the ionic/electrical properties of devices, offering a simple yet potent heterostructure framework that paves the way for further advanced fundamental studies as well as potential applications in optoelectronics, integrated circuits, and neuromorphic computing.

Experimental Procedures

Resource Availability

Lead contact

Further information and requests for resources should be directed to and will be fulfilled by the lead contact, Letian Dou (dou10@purdue.edu).

Materials availability

This study did not generate new unique materials.

Data and code availability

All data are available upon reasonable request.

Preparation of 2D perovskite single crystal heterostructures: The floating growth method was used to obtain 2D halide perovskite nanocrystals. Specifically, PbI_2 or $PbBr_2$ (0.4 mmol) and PEAI or PEABr (0.4 mmol) precursors were dissolved into an acid mixture containing 0.9 mL of HBr or HI and 0.1 mL of H_3PO_2 in a 10 mL glass vial for $(PEA)_2PbI_4$ (I n=1) and $(PEA)_2PbBr_4$ (Br n=1). PbI_2 (0.4 mmol), PEAI (0.2 mmol), and MAI (0.6 mmol) precursors were dissolved into the same acid mixture for $(PEA)_2(MA)Pb_2I_7$ (I n=2). With magnetic stirring, the vial was heated to 120 °C in an oil bath. The $(PEA)_2PbI_4$ (I n=1) solution was cooled down to 55°C, while $(PEA)_2PbBr_4$ (Br n=1) solution was cooled down to 40°C, and $(PEA)_2(MA)Pb_2I_7$ (I n=2) was cooled down to 47°C. The solutions were kept at that temperature in a closed vial as the stock solution. Two microliters of these warm supernatant solution were collected and dispensed with a 10μl pipette onto a glass slide placed in open ambient environment. Single crystal sheets were picked up by PDMS from the solution surface. Single crystal sheets were then transferred from the PDMS to the desired substrate and constructed into a heterostructure through point-to-point transfer using an in-house built transfer equipment.

Single crystal and heterostructure device fabrication: The Ti (4 nm) /Au (30 nm) electrode for contact pads on Si/SiO_2 (300 nm) wafer were prepared by conventional photolithography and thermal evaporation method. The 2D single crystals on PDMS substrates were transferred between the contact pad electrodes and then a PMMA

film with Au electrodes were transferred on these crystals using transfer stage below 85°C. For PMMA film with Au electrodes, following the patterning process of photoresist (AZ 1518), a 130 nm Au was thermally evaporated onto the Si/SiO_2 (300 nm) wafer, followed by hot acetone washing to remove the photoresist. Afterward, the self-assembly monolayer surface treatment of Hexamethyldisilane (HMDS) was applied in vacuum chamber. Subsequently, a PMMA solution was spin-coated on top of the Au electrodes and annealed at 180°C for 10 min. The Au electrodes / PMMA layer were lifted off from substrate and transferred on to the crystals by using thermal release tapes.

Optical microscopy measurements: All bright-field images were collected with a custom Olympus BX53 microscope. All PL images were taken using a X-Cite Series 120 Q lamp as the excitation source. PL spectra were collected with a SpectraPro HRS-300 spectrometer.

Confocal photoluminescence (PL) mapping: A Leica SP8 inverted laser scanning confocal microscope with a 405 nm laser line as the excitation wavelength was used for the PL mapping of the bromide and iodide layers in the vertical heterostructure.

Scanning electron microscopy (SEM) imaging: SEM and EDX mapping images were obtained using a Hitachi S-4800 cold SEM microscope with EDX.

Crystal thickness measurements: The height profile of the crystals was measured using stylus profilometer (DektakXT).

Electrical measurements: The measurement of current-voltage characteristics and bias input for single-crystal devices and single-crystal heterostructure devices were conducted under ambient conditions using Keithley 2400 and Keithley 4200-SCS semiconductor parametric analyzers.

X-ray Diffraction (XRD) pattern measurements: XRD was measured using a powder X-ray diffractometer (Panalytical Empyrean) with a Cu Kα source.

Conductive atomic force microscopy (CAFM) measurements: CAFM images were obtained using the Asylum Research Cypher ES Environmental AFM in the air. The samples for CAFM measurements were prepared on Si/SiO_2 wafers with Ti/Au electrode as a conductive substrate with insulating layer. The 2D perovskite crystal was electrically grounded with a conductive sample holder. One side of crystals was connected to Ti/Au electrode by transferring Au electrode and Ti/Au electrode was connected to Si layer by silver paste. The AFM tips used during the measurement were Ti/Pt-coated AC240TM-R3 tips (Oxford Instruments). The measurements were conducted in the dark under 1 V bias.

Infrared microscope temperature mapping: The thermal behavior of the device is measured using an infrared (IR) microscope (Infrascope™, Quantum Focus Instruments). This IR microscope is configured with adaptable lenses that enable measurements at different spatial resolutions ranging from 105 to 1.8 μm/pixel, and imaging sensor with 1024 × 1024 pixels. In this research, a 12x magnification objective infrared lens is utilized, resulting in an approximate spatial resolution of 2.7 μm/pixel and offering a field of view of about 1 × 1 mm to measure the surface temperature response of the device. Here, the temperature measurement is performed assuming a constant emissivity of 0.8 across the device surface. The transient spatial temperature evolution in the device is recorded in the form of a thermal movie over the 50 second period over which the electric bias is applied, at a temporal resolution of 500 millisecond between each temperature frame. The temperature data is imported in MATLAB for further processing and analysis.

Ion migration simulations: We use our self-consistent numerical simulation (implemented in COMSOL Multiphysics) to investigate the formation of heterojunction at the interface between Br n=1 and I n=1. For simulating the charge transport behavior, we have considered a 2D device structure and self-consistently simulated Poisson's (Eq. 1) and diffusion equations (Eq. 2 and 3) for ionic (cations and anions) charges. The Poison's equation is,

$$\nabla \cdot (\epsilon \nabla V) = -\rho_{\mathrm{v}} \quad \text{Eq. (1)}$$

where, $\rho_v = q(N_c - N_a)$ and N_c, N_a represent the density of cation, anion, respectively. The solution of Poisson's equation provides the time evolution of the electric field ($E = -\nabla V$) depending on the spatial and temporal charge profile in the simulation domain. The solution of Poisson's equation provides insights into the time-evolving electric field ($E = -\nabla V$), influenced by the spatial and temporal charge profiles in the simulation domain. The evolving electric field, in tandem with random diffusion, acts as the primary driving force for charge transport.

$$\frac{\partial c_i}{\partial t} + \nabla \cdot J_i = 0 \quad \text{Eq. (2)}$$

$$J_i = -D_i \nabla c_i - z_i u_i F c_i \nabla V \quad \text{Eq. (3)}$$

Here, c_i and z_i represent the concentration and dimensionless charge number of the species i (i.e., N_c, N_a). D_i and μ_i denote the corresponding diffusivity and mobility of the species i, and are connected via the Einstein relationship, $D = \mu kT/q$. F represents the Faraday constant.

The Br n=1 and I n=1 regions is initially assumed to contain a uniform distribution of anions (e.g., Br^- for Br n=1 and I^- for I n=1) along with an equal amount of immobile background cations, ensuring initial charge neutrality. The boundaries at the metal contacts (x=0 for Br n=1 region and x=L for I n=1 region), including all other external boundaries of the simulation domain, are considered insulating for both anions and cations (i.e. $n \cdot J_i = 0$), thereby allowing the ionic transport only across the junction interface.[47] Additionally, a potential barrier is assumed for charge carriers to traverse between the Br n=1 and I n=1 regions. The mobile concentration values of halide anions used as initial condition were derived from a previous study.[48]

Diode device simulations: The device simulation has been performed using the following analytical equation:[44,45]

$$I = A\,(e^{BV} - 1),\ A = I_s \text{ and } B = \frac{1}{\frac{\eta KT}{q}} \quad .$$

An assumption is made that a tunneling phenomenon occurs across the P-N junction, as the diode operates at a significantly lower turn-on voltage compared to the conventional turn-on voltage of a diode. The physical phenomenon of tunneling is due to the presence of a prefactor (B) within the exponential component. The process involves the regulation of electron transfer from the bromide side to the iodide side, or the movement of holes from the iodide side to the bromide side. The estimated values for variables A and B are 372 and 0.56, respectively. The asymmetry of current in both directions can be attributed to the disparity in bandgap between two crystal sheets. The energy band levels of $(PEA)_2PbBr_4$ and $(PEA)_2PbI_4$ were adapted from previous literature.[43,49]

Acknowledgements

This work is supported by the U.S. National Science Foundation under award no. 2143568-DMR (ion diffusion characterization), the U.S. Department of Energy's Office of Energy Efficiency and Renewable Energy (EERE) under the Solar Energy Technologies Office award DE-EE0009519 (device fabrication and characterization), and the U.S. Department of Energy, Office of Basic Energy Sciences under award DE-SC0022082 (heterostructure synthesis). J.Y.P. acknowledges support by the Bilsland Dissertation Fellowship of Purdue University.

Author Contributions

J.P. and Y.H.L carried out the synthesis of materials, fabrication of devices, characterization, and overall data analysis. M.A.Z.M., M.M.F.I, and M.A.A. performed the computational modelling of ion transport and device simulations. S.Z. contributed to synthesis of materials. K.M. and J.M. performed atomic force microscopy measurements. A.U.G. and A.M. carried out the device temperature mapping. K.W. and S.J.Y. contributed to device measurements and overall data analysis. J.P., Y.H.L., and L.D. wrote the manuscript; all authors read and revised the manuscript. L.D. supervised the project.

Declaration of Interests

The authors declare no competing interests.

References:

1. Kojima, A., Teshima, K., Shirai, Y., and Miyasaka, T. (2009). Organometal halide perovskites as visible-light sensitizers for photovoltaic cells. J. Am. Chem. Soc. *131*, 6050–6051. 10.1021/ja809598r.
2. Park, J., Kim, J., Yun, H.S., Paik, M.J., Noh, E., Mun, H.J., Kim, M.G., Shin, T.J., and Seok, S. Il (2023). Controlled growth of perovskite layers with volatile alkylammonium chlorides. Nature *616*, 724–730. 10.1038/s41586-023-05825-y.
3. Kim, J.S., Heo, J.M., Park, G.S., Woo, S.J., Cho, C., Yun, H.J., Kim, D.H., Park, J., Lee, S.C., Park, S.H., et al. (2022). Ultra-bright, efficient and stable perovskite light-emitting diodes. Nature *611*, 688–694. 10.1038/s41586-022-05304-w.
4. Xiao, Z., Yuan, Y., Shao, Y., Wang, Q., Dong, Q., Bi, C., Sharma, P., Gruverman, A., and Huang, J. (2015). Giant switchable photovoltaic effect in organometal trihalide perovskite devices. Nat. Mater. *14*, 193–197. 10.1038/nmat4150.
5. Snaith, H.J. (2015). Anomalous Hysteresis in Perovskite Solar Cells. J. Phys. Chem. Lett. *6*, 3808–3814. 10.1021/acs.jpclett.5b01645.
6. Vashishtha, P., and Halpert, J.E. (2017). Field-Driven Ion Migration and Color Instability in Red-Emitting Mixed Halide Perovskite Nanocrystal Light-Emitting Diodes. Chem. Mater. *29*, 5965–5973. 10.1021/acs.chemmater.7b01609.
7. Zhang, Y., Lu, D., Gao, M., Lai, M., Lin, J., Lei, T., Lin, Z., Quan, L.N., and Yang, P. (2019). Quantitative imaging of anion exchange kinetics in halide perovskites. Proc. Natl. Acad. Sci. U. S. A. *116*, 12648–12653. 10.1073/pnas.1903448116.
8. Lai, M., Obliger, A., Lu, D., Kley, C.S., Bischak, C.G., Kong, Q., Lei, T., Dou, L., Ginsberg, N.S., Limmer, D.T., et al. (2018). Intrinsic anion diffusivity in lead halide perovskites is facilitated by a soft lattice. Proc. Natl. Acad. Sci. U. S. A. *115*, 11929–11934. 10.1073/pnas.1812718115.
9. Kim, T., Park, S., Iyer, V., Shaheen, B., Choudhry, U., Jiang, Q., Eichman, G., Gnabasik, R., Kelley, K., Lawrie, B., et al. (2023). Mapping the pathways of photo-induced ion migration in organic-inorganic hybrid halide perovskites. Nat. Commun. *14*, 1846. 10.1038/s41467-023-37486-w.
10. Xu, Z., Kerner, R.A., Berry, J.J., and Rand, B.P. (2022). Iodine Electrochemistry Dictates Voltage-Induced Halide Segregation Thresholds in Mixed-Halide Perovskite Devices. Adv. Funct. Mater. *32*. 10.1002/adfm.202203432.
11. Kerner, R.A., Xu, Z., Larson, B.W., and Rand, B.P. (2021). The role of halide

oxidation in perovskite halide phase separation. Joule *5*, 2273–2295. 10.1016/j.joule.2021.07.011.

12. Yang, S.J., Wang, K., Luo, Y., Park, J.Y., Yang, H., Coffey, A.H., Ma, K., Sun, J., Wieghold, S., Zhu, C., et al. (2023). Two-Factor Phase Separations in Mixed-Halide Quasi-2D Perovskite LEDs: Dimensionality and Halide Segregations. ACS Energy Lett., 3693–3701. 10.1021/acsenergylett.3c01009.
13. Shi, E., Yuan, B., Shiring, S.B., Gao, Y., Akriti, Guo, Y., Su, C., Lai, M., Yang, P., Kong, J., et al. (2020). Two-dimensional halide perovskite lateral epitaxial heterostructures. Nature *580*, 614–620. 10.1038/s41586-020-2219-7.
14. Gao, Y., Shi, E., Deng, S., Shiring, S.B., Snaider, J.M., Liang, C., Yuan, B., Song, R., Janke, S.M., Liebman-Peláez, A., et al. (2019). Molecular engineering of organic–inorganic hybrid perovskites quantum wells. Nat. Chem. *11*, 1151–1157. 10.1038/s41557-019-0354-2.
15. Park, J.Y., Song, R., Liang, J., Jin, L., Wang, K., Li, S., Shi, E., Gao, Y., Zeller, M., Teat, S.J., et al. (2023). Thickness control of organic semiconductor-incorporated perovskites. Nat. Chem. 10.1038/s41557-023-01311-0.
16. Sidhik, S., Wang, Y., De Siena, M., Asadpour, R., Torma, A.J., Terlier, T., Ho, K., Li, W., Puthirath, A.B., Shuai, X., et al. (2022). Deterministic fabrication of 3D/2D perovskite bilayer stacks for durable and efficient solar cells. Science (80-.). *377*, 1425–1430. 10.1126/science.abq7652.
17. Wang, K., Lin, Z.Y., Zhang, Z., Jin, L., Ma, K., Coffey, A.H., Atapattu, H.R., Gao, Y., Park, J.Y., Wei, Z., et al. (2023). Suppressing phase disproportionation in quasi-2D perovskite light-emitting diodes. Nat. Commun. *14*, 1–11. 10.1038/s41467-023-36118-7.
18. Yuan, Y., and Huang, J. (2016). Ion Migration in Organometal Trihalide Perovskite and Its Impact on Photovoltaic Efficiency and Stability. Acc. Chem. Res. *49*, 286–293. 10.1021/acs.accounts.5b00420.
19. DeQuilettes, D.W., Zhang, W., Burlakov, V.M., Graham, D.J., Leijtens, T., Osherov, A., Bulović, V., Snaith, H.J., Ginger, D.S., and Stranks, S.D. (2016). Photo-induced halide redistribution in organic-inorganic perovskite films. Nat. Commun. *7*. 10.1038/ncomms11683.
20. Akriti, Shi, E., Shiring, S.B., Yang, J., Atencio-Martinez, C.L., Yuan, B., Hu, X., Gao, Y., Finkenauer, B.P., Pistone, A.J., et al. (2021). Layer-by-layer anionic

diffusion in two-dimensional halide perovskite vertical heterostructures. Nat. Nanotechnol. *16*, 584–591. 10.1038/s41565-021-00848-w.

21. Akriti, Lin, Z.Y., Park, J.Y., Yang, H., Savoie, B.M., and Dou, L. (2022). Anion diffusion in two-dimensional halide perovskites. APL Mater. *10*. 10.1063/5.0088538.
22. Akriti, Zhang, S., Lin, Z.Y., Shi, E., Finkenauer, B.P., Gao, Y., Pistone, A.J., Ma, K., Savoie, B.M., and Dou, L. (2021). Quantifying Anionic Diffusion in 2D Halide Perovskite Lateral Heterostructures. Adv. Mater. *33*, 1–11. 10.1002/adma.202105183.
23. Kong, Q., Obliger, A., Lai, M., Gao, M., Limmer, D.T., and Yang, P. (2020). Solid-state ionic rectification in perovskite nanowire heterostructures. Nano Lett. *20*, 8151–8156. 10.1021/acs.nanolett.0c03204.
24. Peng, W., Aranda, C., Bakr, O.M., Garcia-Belmonte, G., Bisquert, J., and Guerrero, A. (2018). Quantification of Ionic Diffusion in Lead Halide Perovskite Single Crystals. ACS Energy Lett. *3*, 1477–1481. 10.1021/acsenergylett.8b00641.
25. Pan, D., Fu, Y., Spitha, N., Zhao, Y., Roy, C.R., Morrow, D.J., Kohler, D.D., Wright, J.C., and Jin, S. (2021). Deterministic fabrication of arbitrary vertical heterostructures of two-dimensional Ruddlesden–Popper halide perovskites. Nat. Nanotechnol. *16*, 159–165. 10.1038/s41565-020-00802-2.
26. Liu, Y., Guo, J., Zhu, E., Liao, L., Lee, S.J., Ding, M., Shakir, I., Gambin, V., Huang, Y., and Duan, X. (2018). Approaching the Schottky-Mott limit in van der Waals metal-semiconductor junctions. Nature *557*, 696–700. 10.1038/s41586-018-0129-8.
27. Wang, L., Wang, P., Huang, J., Peng, B., Jia, C., Qian, Q., Zhou, J., Xu, D., Huang, Y., and Duan, X. (2022). A general one-step plug-and-probe approach to top-gated transistors for rapidly probing delicate electronic materials. Nat. Nanotechnol. *17*, 1206–1213. 10.1038/s41565-022-01221-1.
28. García-Batlle, M., Baussens, O., Amari, S., Zaccaro, J., Gros-Daillon, E., Verilhac, J.M., Guerrero, A., and Garcia-Belmonte, G. (2020). Moving Ions Vary Electronic Conductivity in Lead Bromide Perovskite Single Crystals through Dynamic Doping. Adv. Electron. Mater. *6*. 10.1002/aelm.202000485.
29. García-Batlle, M., Mayén Guillén, J., Chapran, M., Baussens, O., Zaccaro, J.,

Verilhac, J.M., Gros-Daillon, E., Guerrero, A., Almora, O., and Garcia-Belmonte, G. (2022). Coupling between Ion Drift and Kinetics of Electronic Current Transients in MAPbBr3 Single Crystals. ACS Energy Lett. *7*, 946–951. 10.1021/acsenergylett.1c02578.

30. Futscher, M.H., Lee, J.M., McGovern, L., Muscarella, L.A., Wang, T., Haider, M.I., Fakharuddin, A., Schmidt-Mende, L., and Ehrler, B. (2019). Quantification of ion migration in CH3NH3PbI3 perovskite solar cells by transient capacitance measurements. Mater. Horizons *6*, 1497–1503. 10.1039/c9mh00445a.
31. Van Reenen, S., Kemerink, M., and Snaith, H.J. (2015). Modeling Anomalous Hysteresis in Perovskite Solar Cells. J. Phys. Chem. Lett. *6*, 3808–3814. 10.1021/acs.jpclett.5b01645.
32. Bertoluzzi, L., Belisle, R.A., Bush, K.A., Cheacharoen, R., McGehee, M.D., and O'Regan, B.C. (2018). In Situ Measurement of Electric-Field Screening in Hysteresis-Free PTAA/FA0.83Cs0.17Pb(I0.83Br0.17)3/C60 Perovskite Solar Cells Gives an Ion Mobility of ~3 × 10-7 cm2/(V s), 2 Orders of Magnitude Faster than Reported for Metal-Oxide-Contacted Perovskite C. J. Am. Chem. Soc. *140*, 12775–12784. 10.1021/jacs.8b04405.
33. Lee, J.W., Kim, S.G., Yang, J.M., Yang, Y., and Park, N.G. (2019). Verification and mitigation of ion migration in perovskite solar cells. APL Mater. *7*. 10.1063/1.5085643.
34. Saketh Chandra, T., Singareddy, A., Hossain, K., Sivadas, D., Bhatia, S., Singh, S., Kabra, D., and Nair, P.R. (2021). Ion mobility independent large signal switching of perovskite devices. Appl. Phys. Lett. *119*. 10.1063/5.0051342.
35. Richardson, G., O'Kane, S.E.J., Niemann, R.G., Peltola, T.A., Foster, J.M., Cameron, P.J., and Walker, A.B. (2016). Can slow-moving ions explain hysteresis in the current-voltage curves of perovskite solar cells? Energy Environ. Sci. *9*, 1476–1485. 10.1039/c5ee02740c.
36. Eames, C., Frost, J.M., Barnes, P.R.F., O'Regan, B.C., Walsh, A., and Islam, M.S. (2015). Ionic transport in hybrid lead iodide perovskite solar cells. Nat. Commun. *6*, 2–9. 10.1038/ncomms8497.
37. Frost, J.M., and Walsh, A. (2016). What Is Moving in Hybrid Halide Perovskite Solar Cells? Acc. Chem. Res. *49*, 528–535. 10.1021/acs.accounts.5b00431.

38. Shao, Y., Fang, Y., Li, T., Wang, Q., Dong, Q., Deng, Y., Yuan, Y., Wei, H., Wang, M., Gruverman, A., et al. (2016). Grain boundary dominated ion migration in polycrystalline organic-inorganic halide perovskite films. Energy Environ. Sci. *9*, 1752–1759. 10.1039/c6ee00413j.
39. Yang, B., Brown, C.C., Huang, J., Collins, L., Sang, X., Unocic, R.R., Jesse, S., Kalinin, S. V., Belianinov, A., Jakowski, J., et al. (2017). Enhancing Ion Migration in Grain Boundaries of Hybrid Organic–Inorganic Perovskites by Chlorine. Adv. Funct. Mater. *27*. 10.1002/adfm.201700749.
40. Wang, K., Wu, C., Jiang, Y., Yang, D., Wang, K., and Priya, S. (2019). Distinct conducting layer edge states in two-dimensional (2D) halide perovskite. Sci. Adv. *5*, 1–11. 10.1126/sciadv.aau3241.
41. Euvrard, J., Yan, Y., and Mitzi, D.B. (2021). Electrical doping in halide perovskites. Nat. Rev. Mater. *6*, 531–549. 10.1038/s41578-021-00286-z.
42. Song, J., Qian, J., Liu, L., Huang, D., Li, Z., Xu, B., and Tian, W. (2021). Theoretical study on defect properties of two-dimensional multilayer Ruddlesden-Popper lead iodine perovskite. Comput. Mater. Sci. *194*, 110457. 10.1016/j.commatsci.2021.110457.
43. Silver, S., Yin, J., Li, H., Brédas, J.L., and Kahn, A. (2018). Characterization of the Valence and Conduction Band Levels of n = 1 2D Perovskites: A Combined Experimental and Theoretical Investigation. Adv. Energy Mater. *8*, 1–7. 10.1002/aenm.201703468.
44. Weir, B.E., Alam, M.A., and Silverman, P.J. (2001). Soft breakdown at all positions along the N-MOSFET. Microelectron. Eng. *59*, 17–23. 10.1016/S0167-9317(01)00626-8.
45. Alam, M.A., and Smith, R.K. (2003). A phenomenological theory of correlated multiple soft-breakdown events in ultra-thin gate dielectrics. IEEE Int. Reliab. Phys. Symp. Proc. *2003-January*, 406–411. 10.1109/RELPHY.2003.1197782.
46. Cheng, J., Ma, Y., Zhou, W., Zhang, T., Li, W., Zhang, X., and Yan, H. Universal microscopic patterned doping method for perovskite enables ultra- fast , self-powered ultrasmall perovskite photodiode. 1–24. 10.1002/adma.202300691.
47. Mamun, M.A.Z., Mavinkurve, A., Van Soestbergen, M., and Alam, M.A. (2023). Transient Leakage Current as a Non-destructive Probe of Wire-bond Electrochemical Failures. IEEE Int. Reliab. Phys. Symp. Proc. *2023-March*, 1–

7. 10.1109/IRPS48203.2023.10117658.

48. Bertoluzzi, L., Boyd, C.C., Rolston, N., Xu, J., Prasanna, R., O'Regan, B.C., and McGehee, M.D. (2020). Mobile Ion Concentration Measurement and Open-Access Band Diagram Simulation Platform for Halide Perovskite Solar Cells. Joule *4*, 109–127. 10.1016/j.joule.2019.10.003.

49. Silver, S., Dai, Q., Li, H., Brédas, J.L., and Kahn, A. (2019). Quantum Well Energetics of an n = 2 Ruddlesden–Popper Phase Perovskite. Adv. Energy Mater. *9*. 10.1002/aenm.201901005.

Figures

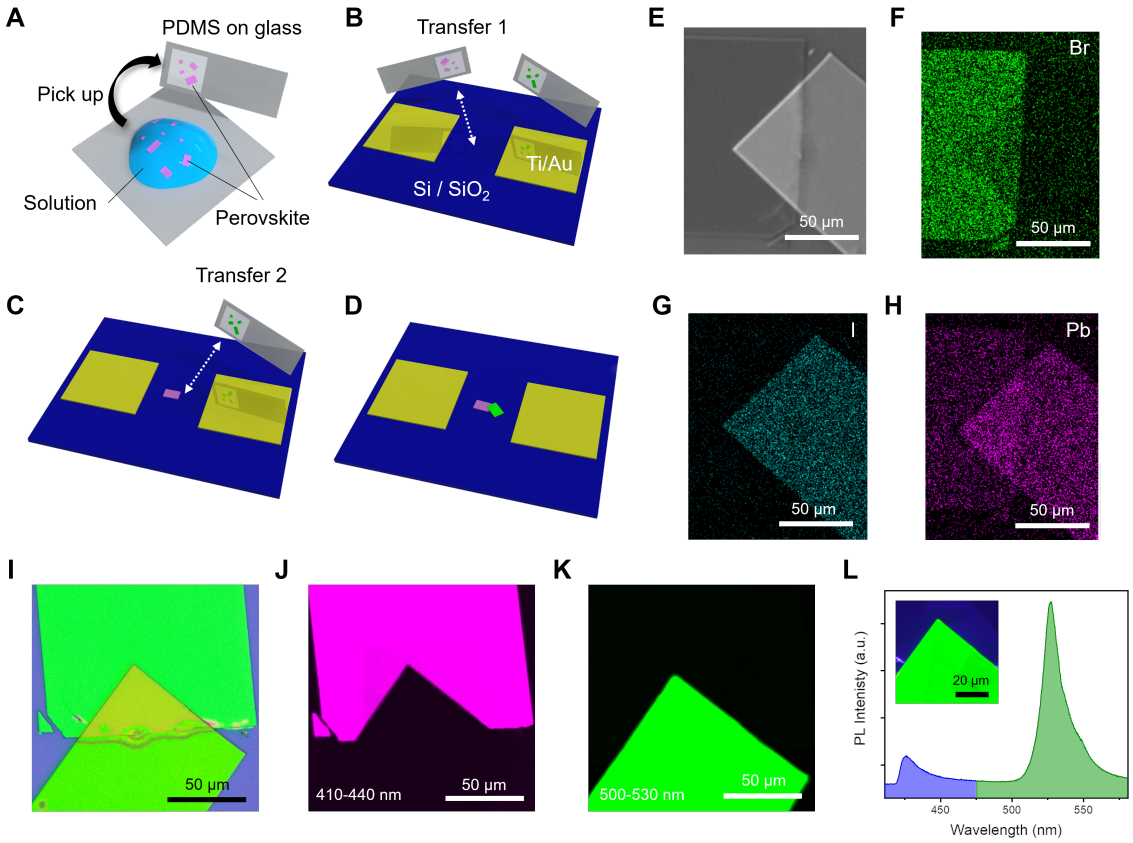

Figure 1. Fabrication scheme and characterization of 2D perovskite heterostructures

(A) Schematic illustration of floating growth method and retrieval of 2D perovskite crystal sheets onto PDMS attached onto a slide glass.

(B-D) Point-to-point multi step dry transfer process of 2D perovskite crystal sheets to create a heterostructure on a Si/SiO_2 substrate prepatterned with Ti/Au pads.

(E) SEM image of a Br n=1 – I n=1 pristine heterostructure.

(F-H) Corresponding SEM EDX images showing the elemental mapping of Br (F), I (G), and Pb (H).

(I) Optical image of the same heterostructure.

(J-K) Confocal PL mapping images showing emissions in the wavelength range of 410 nm-440 nm (J) and 500-530 nm (K).

(L) PL image (inset) and PL spectra captured from the heterostructure junction area.

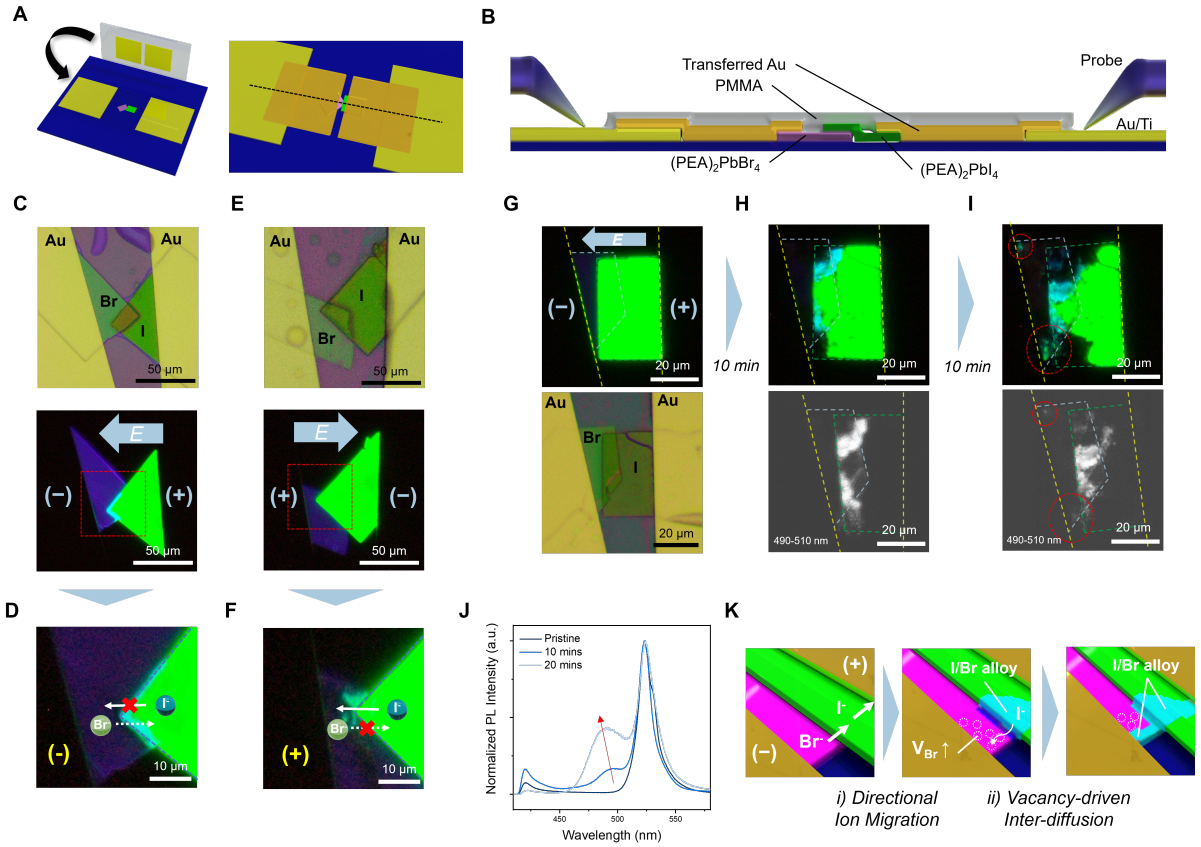

Figure 2. Fabrication of heterostructure device and observation of electrically induced ion migration behavior

(A) Schematic illustration of gold electrode transfer onto 2D perovskite heterostructure.

(B) Cross-sectional schematic representation of the heterostructure device.

(C-E) Two Br n=1 – I n=1 heterostructures induced with opposite direction of electric bias of 5 V for 5 mins with optical and PL images of heterostructures before (C), after (D) electric field towards left, before (E), and after (F) electric field towards right.

(G-I) Br n=1 – I n=1 heterostructure induced with electric bias of 20 V for 20 mins with PL image in its pristine state (G), 10 mins (H), and 20 mins (I) after bias. Downside panel shows the bright field image of the device and confocal PL mapping capturing 490 – 510 nm emission for each corresponding time step.

(J) PL spectra evolution over time.

(K) illustration of the proposed mechanism including directional ion migration and vacancy-driven inter-diffusion in 2D perovskite heterostructures under electric bias.

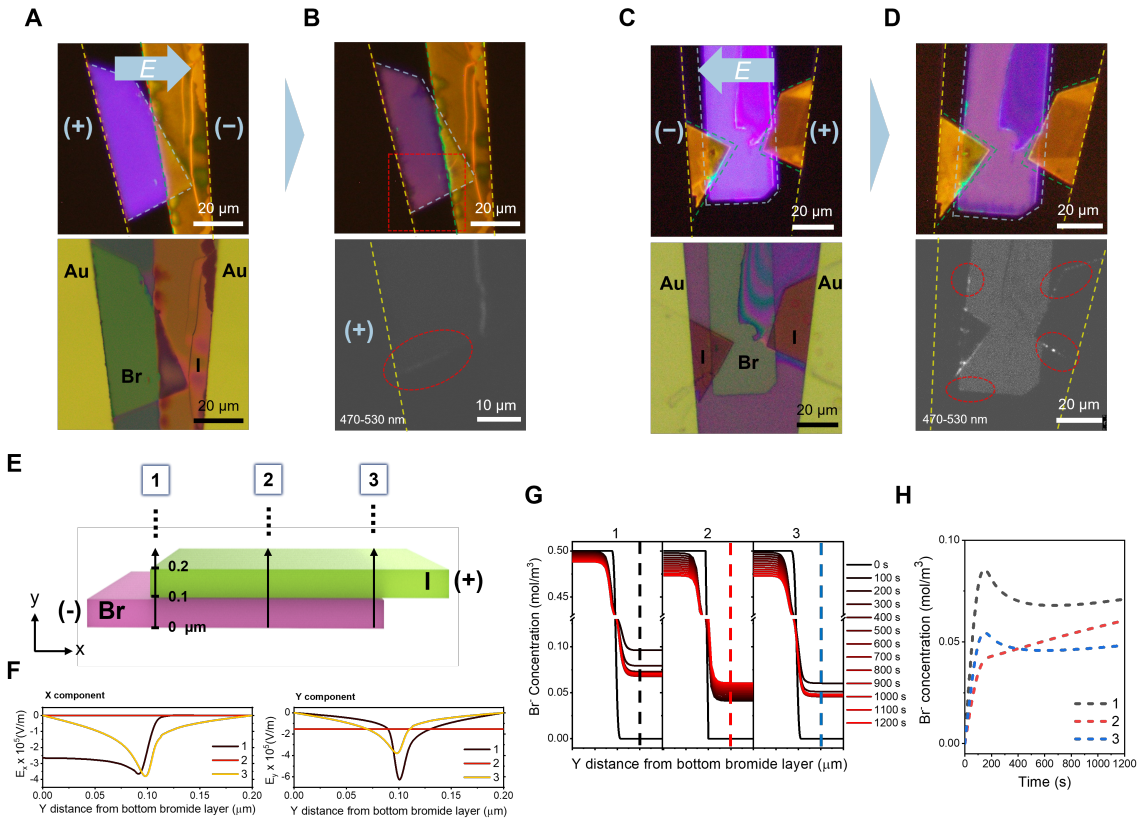

Figure 3. Edge-focused ion migration pathways

(A-B) Br n=1 – I n=2 heterostructure induced with electric bias of 3 V for 5 mins with PL images of heterostructures before (A) and after electric bias (B). Downside panels each show bright field image of the device in (A) and confocal PL mapping image in (B).

(C-D) I n=2 – Br n=1 – I n=2 heterostructure induced with electric bias of 3 V for 5 mins with PL images of heterostructures before (C) and after (D) electric bias. Downside panels each show bright field image of the device in (C) and confocal PL mapping image in (D).

(E) Schematic illustration of the Br n=1 – I n=1 heterostructure under electric bias which was employed for the ion transport modelling. 3 points denoted as 1, 2, and 3 were chosen across the 2D cross-section of the heterostructure as shown. Electric field (x & y components), bromide, and iodide concentration profiles were calculated at each point from bottom to top.

(F) Initial electric field x component (top panel) and y component (bottom panel) at 3 points (1, 2, and 3) in the heterostructure.

(G) Bromide concentration profile evolution in 3 points (1, 2, and 3) from 0 seconds to

1200 seconds with data every 100 seconds shown. A break in the Y axis was applied to better display the data.

(H) Bromide concentration evolution from each point at Y = 0.15 μm (I n=1 side, represented as dashed lines in (G)) plotted against time showing the sharp initial rise followed by a gradual decrease of bromide concentration in points 1 and 3 versus a relatively slow gradual increase of bromide concentration in point 2.

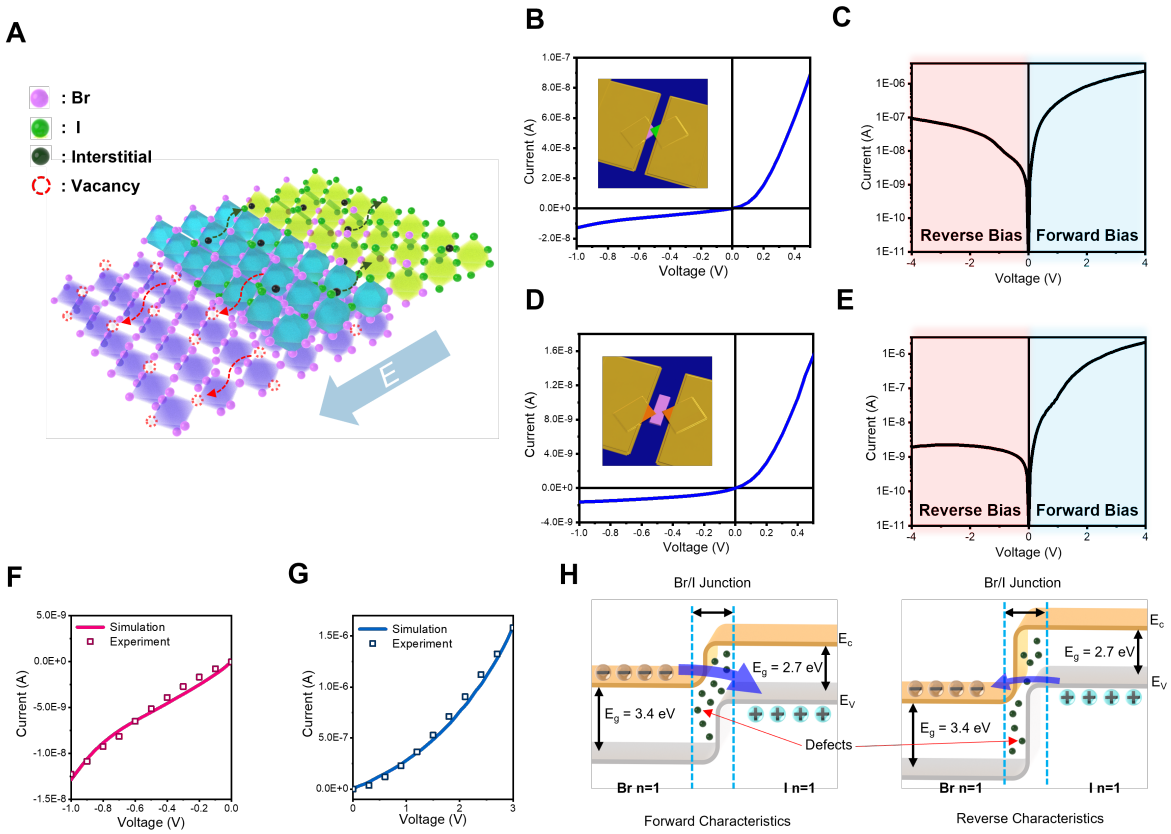

Figure 4. Post-migration diode behavior in heterostructure devices

(A) Schematic illustration showing the drift of halide anions, vacancies, and interstitials in a 2D perovskite heterostructure with respect to electric field.

(B-C) *I-V* curve of a single junction heterostructure device in linear (B) and logarithmic (C) y-axis scale.

(D-E) *I-V* curve of a double junction heterostructure device in linear (D) and logarithmic (E) y-axis scale. Insets show illustrations of the single (B) and double (D) junction device.

(F-G) Simulated *I-V* curves of a single junction heterostructure device in the reverse (F) and forward (G) bias range compared with experimentally obtained results.

(H) Energy band diagram demonstration of the soft breakdown diode behavior in a Br n=1 – I n=1 heterostructure with multiple defects in the junction region. Electron and hole hopping occurs during forward and reverse biasing when there are multiple defects in the junction (blue arrow).